
RESTORATION ADAPTATION FOR SEMANTIC SEGMENTATION ON LOW QUALITY IMAGES

A PREPRINT

Kai Guan^{1,2}, Rongyuan Wu¹, Shuai Li¹, Wentao Zhu², Wenjun Zeng^{2,*}, Lei Zhang^{1,*}

¹The Hong Kong Polytechnic University ²Eastern Institute of Technology, Ningbo
 {kai11.guan, rong-yuan.wu, novak.li}@connect.polyu.hk
 {wtzhu, wzeng-vp}@eitech.edu.cn, cslzhang@comp.polyu.edu.hk

ABSTRACT

In real-world scenarios, the performance of semantic segmentation often deteriorates when processing low-quality (LQ) images, which may lack clear semantic structures and high-frequency details. Although image restoration techniques offer a promising direction for enhancing degraded visual content, conventional real-world image restoration (Real-IR) models primarily focus on pixel-level fidelity and often fail to recover task-relevant semantic cues, limiting their effectiveness when directly applied to downstream vision tasks. Conversely, existing segmentation models trained on high-quality data lack robustness under real-world degradations. In this paper, we propose Restoration Adaptation for Semantic Segmentation (RASS), which effectively integrates semantic image restoration into the segmentation process, enabling high-quality semantic segmentation on the LQ images directly. Specifically, we first propose a Semantic-Constrained Restoration (SCR) model, which injects segmentation priors into the restoration model by aligning its cross-attention maps with segmentation masks, encouraging semantically faithful image reconstruction. Then, RASS transfers semantic restoration knowledge into segmentation through LoRA-based module merging and task-specific fine-tuning, thereby enhancing the model’s robustness to LQ images. To validate the effectiveness of our framework, we construct a real-world LQ image segmentation dataset with high-quality annotations, and conduct extensive experiments on both synthetic and real-world LQ benchmarks. The results show that SCR and RASS significantly outperform state-of-the-art methods in segmentation and restoration tasks. Code, models, and datasets will be available at <https://github.com/KaiGuan/RASS.git>.

Keywords Semantic Segmentation, Image Restoration, Deep Learning

1 Introduction

Semantic segmentation [1–4] is one of the prominent research topics in computer vision, while pixel-level categorization of visual content is crucial for various applications, such as scene understanding [5–7]. Starting with Fully Convolutional Networks (FCNs) [8], pixel-by-pixel classification models have been widely used in semantic segmentation. CNN-based models achieve segmentation by extracting hierarchical features from images through convolutional layers, followed by downsampling and upsampling processes that enable dense pixel-wise classification [9–11]. Later, transformer-based models, such as SegFormer [12] and Mask2Former [2], have achieved state-of-the-art (SOTA) performance on semantic segmentation tasks. Dividing images into patches (tokens) and using self-attention to capture global context and relationships between tokens, these architectures allow for a more nuanced categorization of image regions [1, 2, 13].

Current segmentation models, including those CNN-based [8, 14] and Transformer-based [2, 12] ones, are primarily trained on clear standard-quality (SQ) images. However, the captured images in real-world applications are often subjected to various image degradations [15, 16]. Although [17] extended the general segmenter SAM [18] to multiple single degradation type images, including blur, noise, *etc*, real-world degradation types are often complex and unpredictable, and research on semantic segmentation under such conditions remains limited. Some feature-refinement methods [19, 20] have been proposed to improve segmentation by increasing spatial resolution, but their effectiveness

*Corresponding authors.

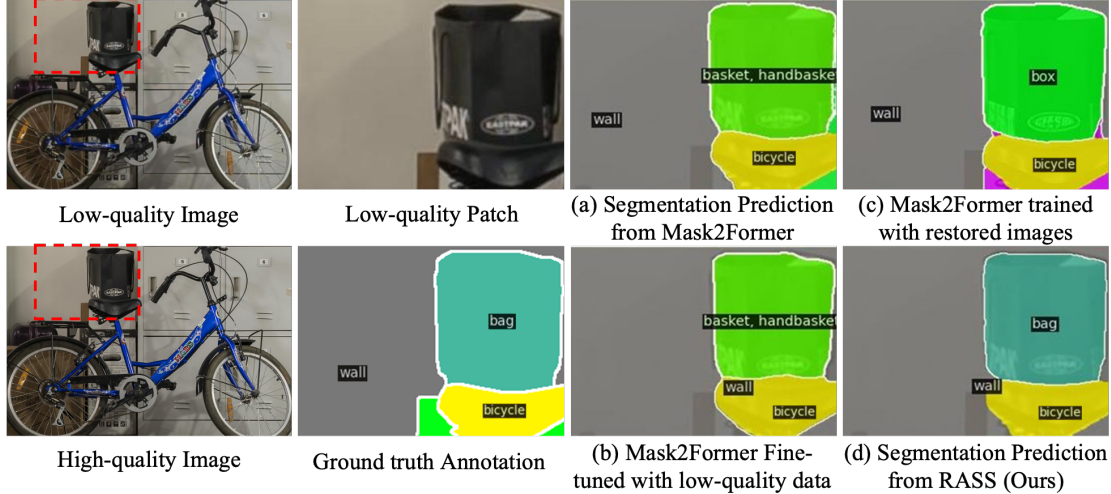


Figure 1: Our RASS framework integrates semantic-guided recovery into the segmentation backbone for robust parsing of low-quality images. (a) Mask2Former [2] trained on high-quality data fails to segment degraded regions (e.g., blurred objects like bag). (b) Fine-tuning on low-quality data recovers coarse structure but struggles with ambiguous targets due to inconsistent features. (c) Restoration as preprocessing can enhance image clarity, but generation without semantic guidance may lead to misclassification (e.g., box). (d) RASS adaptively incorporates restoration into segmentation, better capturing degraded objects while avoiding error propagation from disjoint pipelines.

depends on reliable spatial cues that may be absent under complex corruptions. As illustrated in Fig. 1 (a), directly applying current segmentation models such as Mask2Former [2] to LQ images will struggle in extracting robust features for accurate segmentation. One intuitive solution is to re-train these models on LQ images. However, on the one hand, the architecture design of existing segmentation networks is not suitable for LQ image feature extraction; on the other hand, this solution ignores the exploitation of high-quality (HQ) image priors, which can be used to improve the quality of LQ images and consequently enhance the segmentation performance. As illustrated in Fig. 1 (b), the fine-tuned Mask2Former on LQ images still yields unsatisfactory results.

Restoring HQ images from LQ images has been a long-standing research topic in low-level vision [15, 16, 21], while real-world image restoration (Real-IR) techniques have recently made significant progress [22–25]. Using image restoration as a pre-processing step for semantic segmentation training is a straightforward idea: first enhance the quality of degraded images and then feed them into the segmentation model as training data. However, with this approach, the segmentation results will largely depend on the reliability of the restoration process, leading to suboptimal segmentation performance [26]. As illustrated in Fig. 1(c), the ‘bag’ on the bicycle is mistakenly restored with the shape and texture of a ‘box’, despite the overall improvement in image clarity. This over-generation of incorrect details, however, undermines the subsequent segmentation, leading to misclassification.

Recently developed Stable Diffusion (SD) [27] based generative Real-IR models have demonstrated strong capability to restore HQ images from LQ inputs [28–32]. While Wu *et al.* [29] showed that SD-based generative restoration can benefit LQ image segmentation tasks, the over-generated details can distort the underlying image structure and introduce noticeable visual artifacts. Furthermore, these SD-based Real-IR models often suffer from mismapping and weak spatial alignment due to their reliance on text prompts without explicit semantic or spatial guidance, ultimately resulting in semantically incorrect outputs. Such limitations significantly hinder their effectiveness in downstream segmentation tasks. Some researchers have explored the integration of restoration into the segmentation model training process. For example, Niu *et al.* [33] cascaded the restoration network and the segmentation network during training, while Lee *et al.* [34] proposed FREST, which aims to address the challenge of adverse conditions, by learning an additional embedding space. However, these approaches typically rely on auxiliary restoration modules or multi-stage training objectives to learn feature alignment, rather than leveraging semantically rich pre-trained generative priors for a unified segmentation model.

In contrast to Real-IR, which aims to reconstruct perceptually realistic HQ images from real-world LQ inputs, our objective is to directly obtain accurate semantic segmentation maps from these LQ images containing composite and unknown degradations, rather than merely addressing images with noise or other single degradation types. In this paper, we propose Restoration Adaptation for Semantic Segmentation (RASS) on LQ images, a novel framework that

effectively integrates image enhancement into the segmentation process to handle de-degradation and segmentation simultaneously, achieving robustness to real-world degradations via high-order synthesis generalization. RASS does not treat restoration as a pre-processing step, but instead fuses pretrained restoration parameters into the segmentation model to enhance robustness to LQ conditions. Although training remains sequential, RASS fuses restoration knowledge into the backbone via LoRA so that, at inference, the segmentation head operates on “cleaned” latent features, thereby avoiding error propagation caused by re-encoding intermediate restored pixels. To build a unified framework of restoration and segmentation, we adopt the SD model as backbone. While existing SD-based restoration models focus on fine-grained textures, they often damage structure and cause artifacts. We propose a Semantic-Constrained Restoration (SCR) model to mitigate these issues by guiding restoration with semantic awareness. RASS then leverages LoRA-based fine-tuning to transfer restoration knowledge into segmentation, enhancing robustness to degradation without retraining from scratch. The main contributions of this work are summarized as follows:

- We propose RASS, which, to the best of our knowledge, is the first framework designed to address semantic segmentation of real-world LQ images.
- We propose SCR, injecting segmentation priors by aligning cross-attention maps with semantic masks to recover visually and semantically consistent content.
- We present a carefully annotated real-world LQ segmentation dataset for comprehensive evaluation. Extensive experiments show RASS outperforms existing models on both synthetic and real-world data, with SCR also improving results on the Real-IR benchmark.

2 Related Work

We conduct the literature review from the perspectives of image segmentation and image restoration. Specifically, we supplement the literature review of SQ image segmentation, as it is the foundation and technical support for LQ image segmentation models. Given the strong capabilities of SD-based Real-IR models, our review of image restoration primarily focuses on this line of research.

Standard Quality Image Segmentation: Segmentation on SQ images has been extensively studied. Starting from FCN [8], which enables pixel-wise prediction using fully convolutional networks, many CNN-based methods have been developed to improve accuracy and efficiency [10, 11, 14]. Transformer-based models, such as SegFormer [12], significantly improve complex scene segmentation by capturing long-range interactions and global context. Mask2Former [2] has achieved a breakthrough in decoder design, which integrates Transformer-based attention mechanisms into a unified framework for instance and demonstrate that, setting new SOTA benchmarks across various datasets. More recently, efficiency-oriented models like FeedFormer [35], SeaFormer [36], and CGRSeg [13] further reduce computation via low-level features, axial attention, or context-guided reconstruction. Despite the impressive performance of current segmentation models, they are primarily trained on SQ images and lack robustness to LQ images, which are common in practical applications. Fine-tuning these models with LQ images may improve robustness but cannot fully address the issue of image degradation. This is because the design of SQ segmentation models relies on extracting discriminative features from images, which are obscured by the unknown degradation in LQ images.

Low Quality Image Segmentation: Recent efforts have explored LQ segmentation. One intuitive approach is to restore images before segmentation. For instance, SR4IR [37] adopts task-guided super-resolution to improve segmentation performance. However, restoration as a pre-processing step is often sub-optimal. Another strategy is using knowledge distillation to extract features from a model trained on HQ images to assist segmentation on degraded images. Guo *et al.* [26] and Endo *et al.* [38] used models trained on clean images as teacher networks to assist LQ image segmentation models. Yet, performance is limited by the teacher’s capacity and domain gap. More recently, some researchers have attempted to collaboratively perform semantic segmentation and image restoration. Lee *et al.* [34] proposed FREST for semantic segmentation under adverse conditions, which learns a condition-specific embedding space to restore features in degraded images, simulating normal conditions. Nevertheless, degradation types under adverse environmental conditions are more predictable than in real-world scenarios, while introducing an additional restoration module increases training cost.

Real-World Image Restoration: Recent advances have explored diffusion models for real-world image restoration, particularly leveraging pre-trained text-to-image (T2I) models like Stable Diffusion for their strong generative priors [29, 30, 39, 40]. Early methods such as StableSR [30] and DiffBIR [31] introduce trainable encoders or two-stage pipelines to adapt SD for LQ inputs. SeeSR [29] enhances semantic alignment using degradation-aware prompts and semantic cues, while OSEDiff [40] improves efficiency via direct LQ input for one-step inference. PiSA-SR [32] separates pixel- and semantic-level objectives using dual LoRA modules, enabling controllable restoration. However, these models rely heavily on text prompts without explicit semantic or spatial guidance, often resulting in misaligned

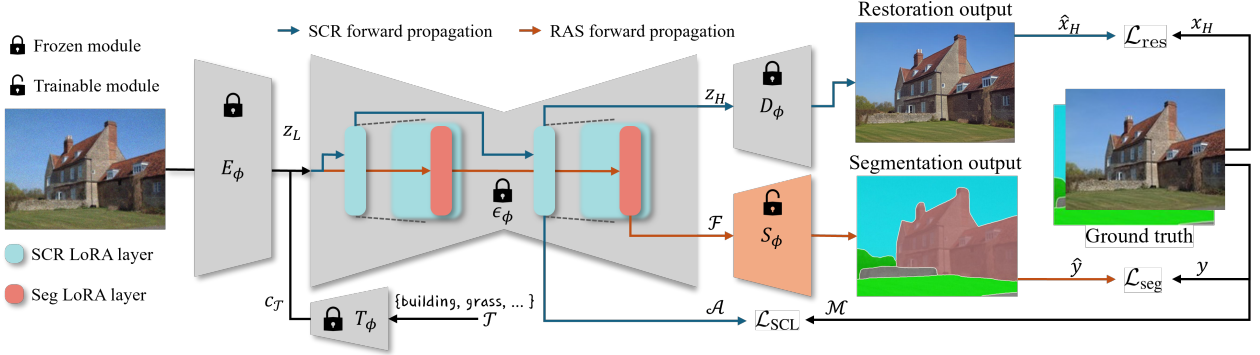


Figure 2: Overview of our RASS training framework. A pre-trained SD model is used as the backbone. In the first stage, the SCR model is trained by injecting trainable SCR LoRA layers into the pretrained diffusion network ϵ_ϕ . The LQ image is passed through the frozen VAE encoder E_ϕ , a LoRA finetuned diffusion network ϵ_ϕ , and frozen VAE decoder D_ϕ to generate the restored HQ image \hat{x}_H , the given text prompt T is processed by the frozen text encoder T_ϕ to obtain the corresponding text embedding c_T . The restoration is supervised by the loss \mathcal{L}_{res} between \hat{x}_H and the ground truth x_H , along with a Semantic-Constraint loss \mathcal{L}_{SCL} computed from the cross-attention maps \mathcal{A} in SCR LoRA and the semantic masks \mathcal{M} . In the second stage, the learned SCR LoRA weights are merged and used to initialize new trainable Segmentation (Seg) LoRA layers to train the RAS model. Internal features \mathcal{F} from E_ϕ and ϵ_ϕ are fed into a trainable segmentation head S_ϕ , with segmentation loss \mathcal{L}_{seg} to guide the training process. RASS transfers the restoration knowledge to the segmentation task through LoRA-based module merging and task-specific fine-tuning, thus achieving robust segmentation of LQ images.

or semantically incorrect outputs when guidance is insufficient, which may negatively impact downstream tasks like semantic segmentation.

3 Methodology

3.1 Framework Overview

Based on the above literature review, our motivation lies in the observation that image restoration and segmentation are two inherently interconnected tasks, yet they are often treated independently in existing works. Conventional image restoration methods primarily emphasize pixel-level fidelity, neglecting the recovery of task-relevant semantic structures, which limits their utility in supporting downstream vision tasks. On the other hand, segmentation models are typically trained on high-quality images and lack robustness against real-world degradations, resulting in substantial performance degradation when applied to LQ inputs.

The framework of our proposed Restoration Adaptation for Semantic Segmentation (RASS) method is shown in Figure 2. Our framework includes two core models, Semantic-Constrained Restoration (SCR) model and Restoration Adaptation Segmentation (RAS) model. The two models share a backbone, a T2I model with strong semantic priors. We build our framework with LoRA-based models to complete different tasks. In the first stage, we first train SCR. Considering that T2I models usually have problems with mismapping and poor spatial correspondence due to the lack of detailed spatial guidance, we design a semantic-constrained loss to guide the model to accurately find the target area in response to the text. In the second stage, we design a restoration adaptation strategy that effectively transfers restoration knowledge into the segmentation process by merging the LoRA model, thereby enhancing the robustness of RASS to LQ images without introducing additional modules and parameters. RASS does not iteratively use improved segmentation to refine restoration; instead, its restoration process is explicitly guided by semantic cues rather than being purely low-level or task-agnostic.

3.2 Semantic-Constrained Restoration Model

The recently proposed OSEDiff [28] utilizes a single-step diffusion process for end-to-end Real-IR training, enabling the adoption of a residual learning strategy. We denote the LQ and HQ images as x_L and x_H , respectively, and their corresponding latent representations as z_L and z_H . Let E_ϕ , ϵ_ϕ , and D_ϕ represent the VAE encoder, latent diffusion network, and VAE decoder of a pretrained SD model, respectively, where ϕ denotes the model parameters. To adapt SD

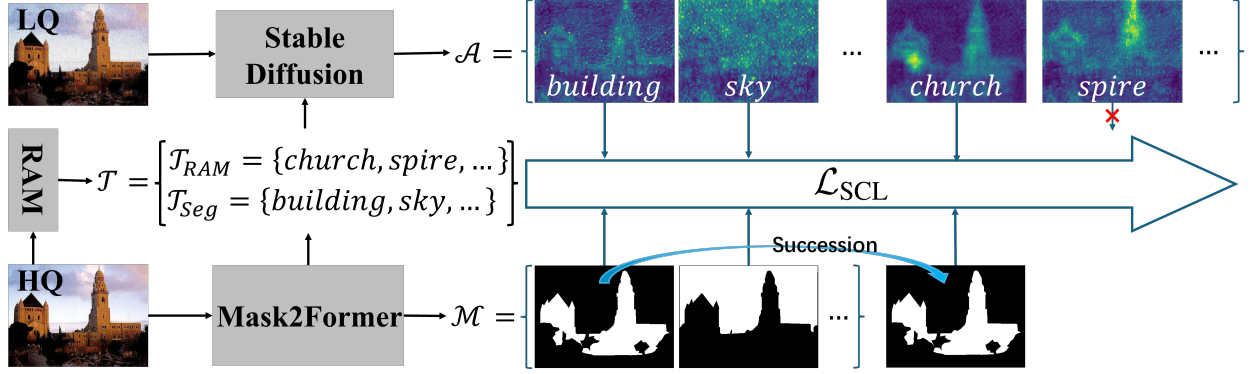


Figure 3: Semantic-Constrained Loss (SCL) computation. Semantically aligned texts inherit corresponding masks (e.g., “church” inherits the mask of “building”), while unmatched terms (e.g., “spire”) are excluded from SCL.

to our task, we freeze the VAE and introduce trainable restoration LoRA modules (*i.e.*, SCR LoRA in Figure 2) into the diffusion network. We fine-tune ϵ_ϕ to $\epsilon_{\theta_{scr}}$ using LoRA [41], where $\theta_{scr} = \{\phi, \Delta\theta_{scr}\}$ and $\Delta\theta_{scr}$ is the SCR-specific LoRA parameter set. Since SD is a text-conditioned model, we extract the text embedding $c_{\mathcal{T}}$ from the input description \mathcal{T} [27], perform the noise prediction as $\hat{\epsilon} = \epsilon_\phi(z_t; t, c_{\mathcal{T}})$, in one-step diffusion model (*i.e.*, timestep $t = 1$), so it can be directly indicated as $\hat{\epsilon} = \epsilon_{\theta_{scr}}(z_L, c_{\mathcal{T}})$. The HQ latent can then be estimated by $z_H = z_L - \hat{\epsilon}$. The general restoration loss function for training SCR LoRA is expressed as follows:

$$\mathcal{L}_{\text{res}}(\hat{x}_H, x_H) = \lambda_{\text{MSE}} \mathcal{L}_{\text{MSE}} + \lambda_{\text{LPIPS}} \mathcal{L}_{\text{LPIPS}}, \quad (1)$$

where \mathcal{L}_{MSE} is the pixel-wise mean squared error between the restored image $\hat{x}_H = D_\phi(z_H)$ and ground truth x_H , encouraging accurate low-level reconstruction. $\mathcal{L}_{\text{LPIPS}}$ denotes the perceptual loss based on deep features from a pretrained network, promoting visually realistic results. We set $\lambda_{\text{MSE}} = 1$ and $\lambda_{\text{LPIPS}} = 2$ to balance pixel-level and perceptual quality, following [28].

To incorporate fine-grained semantic priors into the restoration process, we introduce a Semantic-Constrained Loss (SCL) that guides the SCR LoRA training by aligning cross-attention responses with object-level semantic information. While the base SCR model operates within the latent space of a pretrained SD model, semantic grounding enables it to more accurately restore content relevant to downstream segmentation tasks.

Obtaining precise semantic masks is central to SCL. Open-vocabulary models offer broad category coverage but coarse masks, while closed-set models provide finer masks but cover fewer categories. To balance this trade-off, we find that training our model requires only a small amount of high-quality data (see [Appendix 8.2](#)). We therefore select a subset of semantically rich images based on image quality assessment (IQA) scores and segmentation quality, and combine them with samples from standard segmentation datasets that provide pixel-level annotations. Specifically, we use a pre-trained segmentation model to generate semantic masks $\mathcal{M} = \{M_1, \dots, M_K\}$ and labels $\mathcal{T}_{\text{Seg}} = \{T_1, \dots, T_K\}$ from each high-quality image x_H . To enrich semantic content, we also use RAM [42] to extract additional descriptive labels $\mathcal{T}_{\text{RAM}} = \{T_1, \dots, T_L\}$ from the same image. The combined label set $\mathcal{T} = \mathcal{T}_{\text{Seg}} \cup \mathcal{T}_{\text{RAM}}$ is encoded via CLIP’s text encoder to obtain the semantic representation $c_{\mathcal{T}}$. Since many tags in \mathcal{T}_{RAM} are overlapping or closely related to those in \mathcal{T}_{Seg} (*e.g.*, “people” vs. “person”), we manually construct a mapping table (see [Appendix 8.3](#)) to align them, allowing RAM-derived tags to inherit the corresponding masks when applicable (as shown in Figure 3).

During SCR LoRA training, these text queries $c_{\mathcal{T}}$ compute cross-attention with latent visual features from degraded input x_L , producing attention maps $\mathcal{A} = \{A_1, \dots, A_{K+L}\}$, where each A_n (for $n = 1, \dots, K+L$) highlights the spatial region associated with the semantic tag $T_n \in \mathcal{T}$. These attention maps highlight spatial regions in x_L associated with the semantic concept T_n , guiding the model toward generating visually coherent content. While there is a resolution gap between the typically coarse attention maps and higher-resolution ground-truth masks, we treat these attention maps as structural priors rather than pixel-accurate segmentations: they reliably capture the essential spatial topology of semantic regions across scales. The calculation process of SCL is illustrated in Figure 3. It comprises both region-level and pixel-level components, which can explicitly align attention responses with the ground-truth semantic structure, encouraging semantically meaningful focus and enhancing the model’s ability to preserve structural fidelity during restoration. The SCL loss is:

$$\mathcal{L}_{\text{SCL}}(A, M) = \lambda_{\text{region}} \mathcal{L}_{\text{region}} + \lambda_{\text{pixel}} \mathcal{L}_{\text{pixel}}, \quad (2)$$

where λ_{region} and λ_{pixel} are two scaling factors. The region-level loss $\mathcal{L}_{\text{region}}$ encourages the attention map $A \in [0, 1]^{H \times W}$ to focus its activation within the semantic region $M \in \{0, 1\}^{H \times W}$, a binary mask where $M_{i,j} = 1$ indicates object presence:

$$\mathcal{L}_{\text{region}} = 1 - \frac{\sum_{i,j} A_{i,j} \cdot M_{i,j}}{\sum_{i,j} A_{i,j}}, \quad (3)$$

where (i, j) indexes each spatial location, and $A_{i,j} \in [0, 1]$ denotes the normalized attention response at that location. This formulation measures the proportion of attention energy that overlaps with the target region, penalizing dispersed or misaligned responses.

To achieve finer semantic consistency, we use the binary cross-entropy loss as the pixel-level loss $\mathcal{L}_{\text{pixel}}$:

$$\begin{aligned} \mathcal{L}_{\text{pixel}} = -\frac{1}{HW} \sum_{i=1}^H \sum_{j=1}^W & \left[M_{i,j} \log(A_{i,j}) \right. \\ & \left. + (1 - M_{i,j}) \log(1 - A_{i,j}) \right]. \end{aligned} \quad (4)$$

It is important to note that the lengths of M and A are not equal. When computing \mathcal{L}_{SCL} , each pair of $M \in \mathcal{M}$ and $A \in \mathcal{A}$ is matched based on the associated tag T . Attention maps A without a corresponding semantic mask M are excluded from the loss computation. In summary, SCL is implemented as a multi-resolution-layer constraint that aligns coarse attention responses from multiple transformer layers with the corresponding semantic masks; this provides explicit structural regularization during training and helps to suppress spurious activations across layers.

The total objective for the SCR model is the direct sum of the restoration loss and the semantic-constrained loss, as the specific weighting is handled internally within the SCL components (λ_{region} and λ_{pixel}):

$$\mathcal{L}_{\text{total}} = \mathcal{L}_{\text{res}} + \mathcal{L}_{\text{SCL}}. \quad (5)$$

3.3 Restoration Adaptation Segmentation Model

High-quality visual representations are crucial for achieving accurate semantic segmentation, especially when the input images suffer from severe degradations. To this end, we first conduct a restoration-focused pretraining stage, where the model learns to reconstruct clean images from their degraded counterparts. This restoration stage significantly enhances the perceptual quality and structural consistency of the intermediate features, which are essential for downstream dense prediction tasks such as segmentation.

To effectively transfer restoration knowledge to the segmentation task, we propose a Restoration Adaptation Segmentation (RAS) model based on the LoRA framework. Specifically, the SCR LoRA parameters $\Delta\theta_{\text{scr}}$, trained during the restoration stage to handle various degradation types, are integrated into the backbone network as its initialization. Consequently, the latent diffusion network is initialized with $\epsilon_{\theta_{\text{scr}}}$, replacing the original ϵ_{ϕ} . On top of this restored backbone, we introduce an Seg LoRA branch dedicated to segmentation, denoted as $\Delta\theta_{\text{seg}}$, which is fine-tuned specifically for the downstream segmentation task, as illustrated in Figure 2. The complete parameter set of RASS is therefore defined as $\theta_{\text{rass}} = \{\phi, \Delta\theta_{\text{scr}}, \Delta\theta_{\text{seg}}\}$. This modular design enables the seamless transfer of degradation-invariant features learned during restoration to the segmentation stage, thereby enhancing the model's capacity to extract semantically meaningful representations from LQ inputs.

Unlike restoration models, segmentation models do not require the ϵ_{ϕ} to predict noise $\hat{\epsilon}$, nor do they rely on the D_{ϕ} to reconstruct the HQ image from the refined latent representation. Instead, existing segmentation frameworks typically depend on multi-scale feature representations to achieve accurate pixel-wise classification. To this end, during the Seg LoRA training phase, we replace the D_{ϕ} with a trainable segmentation head, denoted as S_{ϕ} , which takes as input the hierarchical features $\mathcal{F}_{\epsilon} = \{f_{\epsilon}^{(i)}\}_{i=1}^{N_{\epsilon}}$ extracted from the latent diffusion network and predicts the corresponding segmentation mask. In addition, we incorporate features $\mathcal{F}_E = \{f_E^{(i)}\}_{i=1}^{N_E}$ extracted from E_{ϕ} into S_{ϕ} . This is because the latent space is inherently compressed and may lose important fine-grained details, while the encoder features can help retain spatial precision and structural information crucial for accurate segmentation. To supervise this process, we adopt a compound segmentation loss \mathcal{L}_{seg} composed of classification and mask-matching objectives:

$$\mathcal{L}_{\text{seg}}(\hat{\mathbf{y}}, \mathbf{y}) = \lambda_{\text{CE}} \mathcal{L}_{\text{CE}} + \lambda_{\text{Dice}} \mathcal{L}_{\text{Dice}} + \lambda_{\text{cls}} \mathcal{L}_{\text{CE}}^{\text{cls}}, \quad (6)$$

where $\hat{\mathbf{y}} = S_{\phi}(\mathcal{F}_{\epsilon}, \mathcal{F}_E)$ denotes the predicted segmentation mask, \mathbf{y} is the ground-truth segmentation mask, \mathcal{L}_{CE} is the binary cross-entropy loss applied to predicted masks, and $\mathcal{L}_{\text{Dice}}$ is the soft Dice loss [43] promoting spatial overlap with ground-truth masks. The term $\mathcal{L}_{\text{CE}}^{\text{cls}}$ denotes classification loss used for category prediction. Following settings in [2], we set $\lambda_{\text{CE}} = \lambda_{\text{Dice}} = 5.0$ and $\lambda_{\text{cls}} = 2.0$. For unmatched predictions, a reduced weight $\lambda_{\text{cls}} = 0.1$ is applied to mitigate overfitting on background categories.

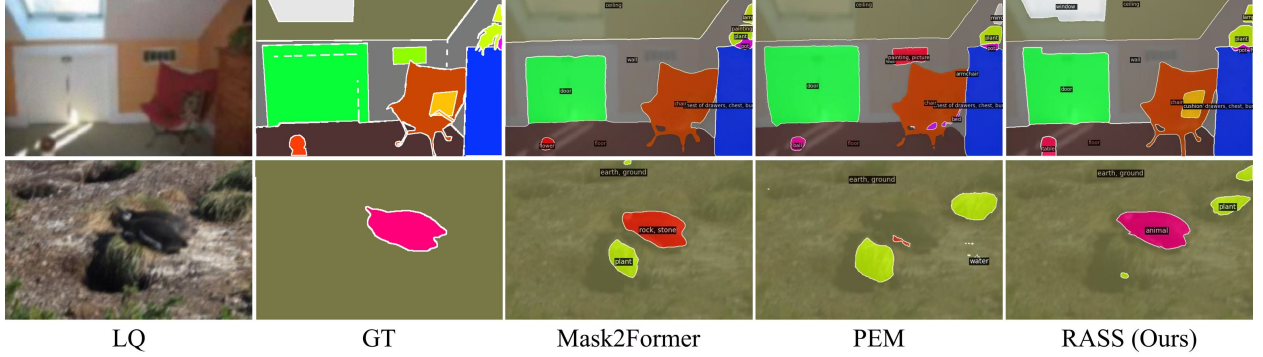


Figure 4: Comparison of segmentation results of different methods, the above samples are from the simulated degradation ADE20K (first row) and RealLQ (second row) dataset. The comparison models are fine-tuned with LQ images.

4 Experiments

4.1 Experimental Settings

Training and Testing Datasets. For RASS, we use ADE20K [44] (150 categories) for training and evaluation, applying the Real-ESRGAN [45] degradation pipeline to simulate LQ inputs. We also construct a real-world LQ dataset, namely RealLQ, containing 100 degraded images from RealSR [46], DrealSR [47], and SR-Raw [48], covering various scenes with 82 annotated categories. This dataset is augmented with synthetic LQ data for comprehensive evaluation, and detailed settings are provided in the **Appendix 8.1**. To improve the effectiveness of SCR in RASS, we train on 469 ADE20K images together with 475 curated LSDIR [49] images, using the same degradation pipeline to synthesize LR-HR pairs. Evaluation is conducted on 3,000 synthetic LQ images from DIV2K-Val [50] and real LQ-HQ pairs from DrealSR and RealSR.

Implementation Details. We train the SCR model following the settings of OSEDiff [28], using 8 NVIDIA H20 GPUs for about 1 day with a batch size of 16. The AdamW optimizer [51] is adopted with a learning rate of 5e-5. The model for obtaining semantic masks is Mask2Former [2]. The RAS model uses Mask2Former [2] as the segmentation head and follows its settings for 160,000 iterations on the same hardware setup, using AdamW with an initial learning rate of 1e-4 and weight decay of 5e-2. During inference, $RASS_{base}$ replaces Mask2Former to extract category labels \mathcal{T}_{Seg} . Note that $RASS_{base}$ serves as the baseline version of our RASS, utilizing OSEDiff⁺ (with a frozen VAE encoder) as the restoration adaptation module. Additionally, following the protocol of OSEDiff [28], we use DAPE [29] instead of RAM to generate \mathcal{T}_{RAM} .

Evaluation Metrics. We use mean Intersection over Union (mIoU), a standard metric that measures the overlap between predicted and ground-truth segmentation masks, to evaluate segmentation performance. Frames-per-second (FPS) is measured on an NVIDIA H20 GPU, with a batch size of 1 by taking the average runtime on the entire validation set, including post-processing time. For image quality, we adopt both full-reference and no-reference metrics. PSNR and SSIM [52] measure pixel-level fidelity, while DISTS [53] assesses perceptual quality. NIQE [54], MANIQA [55], MUSIQ [56], and CLIPQA [55] are used as no-reference metrics to evaluate overall image quality.

Compared Methods. For the segmentation task, due to the limited availability of public implementations for LQ image segmentation models and their significantly different performance compared to standard-quality models, we compare with several SOTA segmentation models on standard-quality images, including SegFormer-B5 [12], Mask2Former-L [2], FeedFormer-B2 [35], SeaFormer-L [57], and PEM-L⁺ [58] (enhanced version using swin-L as backbone). All models are fine-tuned on the same training data using their official code and checkpoints. For the generative restoration task, we evaluate SCR against SOTA Real-IR methods, including StableSR [30], SeeSR [29], DiffBIR [31], OSEDiff [28], and PiSA-SR [32], all of which are based on diffusion models. Publicly released codes and models are used for evaluation.

4.2 Comparison with State-of-the-Arts

Quantitative Comparisons. To enable a fair comparison between RASS and SOTA segmentation models on LQ images, we adopt three evaluation protocols. First, in Direct Testing (DT), models trained on SQ data are directly evaluated on LQ images. Second, in Restoration-to-Segmentation (R2S), LQ images are first restored using SCR (chosen for its strong semantic preservation) and then fed into the same models as used in DT. Third, in Fine-Tuning

(FT), models originally trained on SQ data are further fine-tuned using LQ data before being tested on LQ images. Since RASS is trained on LQ data, its DT results are not applicable and thus omitted (denoted by ‘-’ in Table 1). However, since it generalizes well to HQ inputs, its R2S results are reported. In FT, although RASS is not pre-trained on SQ, all models are ultimately trained on LQ data, ensuring a fair comparison.

Table 1: Semantic segmentation (mIoU↑) on degraded ADE20K-val and RealLQ. Symbol ‘+’ denotes an enhanced version, and ‘-’ denotes not applicable. Best results are highlighted in **bold**.

Method	ADE20K			RealLQ			FPS	Params	Params Trainable
	DT	R2S	FT	DT	R2S	FT			
SegFormer [12]	26.37	44.34	34.57	22.54	25.31	22.63	-	84.7M	84.7M
Mask2Former [2]	37.15	45.64	44.19	33.15	34.83	34.41	5.4	215.5M	215.5M
FeedFormer [35]	22.62	41.39	23.98	20.87	21.19	19.19	50.4	29.1M	27.9M
SeaFormer [57]	16.39	38.09	23.24	15.52	17.86	14.97	31.1	14M	14M
PEM ⁺ [58]	33.55	45.54	41.52	33.52	31.80	34.38	9.7	207.1M	207.1M
RASS (Ours)	-	46.81	47.42	-	37.84	39.80	3.4	1788.7M	27.9M

Table 1 summarizes the comparison results, RealLQ shares the same testing resolution and FPS as ADE20K. SegFormer was not benchmarked for FPS in this specific environment due to version limitations and is marked as “-”. All baseline models suffer from significant performance drops under the DT setting, reflecting limited robustness to LQ inputs. In contrast, our RASS achieves the best performance (47.42 mIoU), outperforming the strongest baseline Mask2Former (44.19 mIoU with FT) by 3.23 mIoU. While RASS (1.7B params) operates at 3.4 FPS—slower than Mask2Former (5.4 FPS)—this computational cost is justified by the necessity of capacity: efficiency-focused models like SeaFormer (14M params) fail to handle degradations (only 14.97 mIoU). In addition, although RASS leverages a much larger backbone, our proposed Restoration Adaptation Strategy enables training only 27.9M parameters, which is significantly fewer than Mask2Former’s 215.5M trainable parameters. Importantly, at inference RASS performs only one-step denoising in latent space: the input is encoded by the VAE encoder and denoised by the U-Net, and the resulting cleaned latent features are fed directly to the segmentation head. This avoids running the computationally expensive VAE decoder and reduces inference cost compared to full image reconstruction. Under the R2S protocol, most baselines benefit from enhanced inputs, but RASS remains the top performer (46.81 mIoU). Although baselines improve moderately with fine-tuning, they still lag behind RASS. On the RealLQ dataset, FT does not consistently outperform DT; lightweight models like FeedFormer and SeaFormer even degrade after fine-tuning, possibly due to the domain gap between synthetic degradations in ADE20K and real-world LQ characteristics. Restoration generally improves performance under R2S, except for PEM⁺, which experiences a 1.82 mIoU drop—indicating that restoration may sometimes be detrimental due to residual quality gaps. This highlights the advantage of RASS, which remains effective without relying on the quality of preprocessing. Although Figure 4 shows that RASS performs well, some pixels are still missegmented—for example, the target in the lower-left corner of the first row. This may result from excessive compression of small targets in the latent space, making them harder to recognize.

To demonstrate the effectiveness of our SCR, we conduct a comprehensive performance comparison with other SOTA models on the common RealIR test benchmark. It is worth noting that since our SCR adopts the OSEDiff framework and is trained on the selected dataset with semantic constraints, it inherently supports one-step denoising. As illustrated in Table 2, SCR demonstrates superior no-reference perceptual quality, achieving the highest MUSIQ, MANIQA, and CLIPQA scores on both DrealSR, RealSR and DIV2K, and the best NIQE performance on RealSR while remaining competitive on DrealSR and DIV2K. Furthermore, despite using only a single sampling step and being trained on limited data, SCR attains competitive full-reference performance, ranking among the top in PSNR and SSIM. It outperforms most single-step baselines and approaches multi-step counterparts such as StableSR and SeeSR, effectively balancing perceptual quality and fidelity. The visualization results in Figure 5 show that SCR not only has strong semantic understanding capabilities (recovering the degraded leaf), providing a foundation for RASS, but also surpasses other models in restoring fine texture details (recovering the tiles on the roof).

Additional visual analysis, quantitative results comparing RASS with refinement-based methods, and quantitative results comparing SCR with non-diffusion baselines (e.g., GAN-based methods) are provided in the **Appendix** 8.4 and 8.5.

4.3 Ablation Studies

We conducted ablation studies to validate the contribution of each component in RASS. Additional results, including hyperparameter analysis of SCL, are provided in the **Appendix** 8.2.

Table 2: Quantitative comparison with Diffusion-based methods on DrealSR, RealSR and DIV2K datasets. The suffix -N indicates the number of inference steps (e.g., -200 for 200 steps, -1 for single-step), which affects the inference time and efficiency. Best results are highlighted in **bold**.

Dataset	Method	PSNR \uparrow	SSIM \uparrow	DISTS \downarrow	NIQE \downarrow	MUSIQ \uparrow	MANIQA \uparrow	CLIPQA \uparrow
DrealSR	StableSR-200 [30]	28.03	0.7536	0.2269	6.5239	58.51	0.5593	0.6356
	DiffBIR-50 [31]	26.71	0.6571	0.2748	6.3124	61.07	0.5930	0.6395
	SeeSR-50 [29]	28.14	0.7712	0.2299	6.4523	64.76	0.6005	0.6897
	OSEDiff-1 [28]	27.92	0.7835	0.2165	6.4902	64.65	0.5899	0.6963
	PiSA-SR-1 [32]	28.31	0.7804	0.2169	6.1837	66.10	0.6146	0.6968
	SCR-1 (Ours)	28.16	0.7743	0.2302	6.4616	67.16	0.6394	0.7056
RealSR	StableSR-200 [30]	24.65	0.7080	0.2140	5.8809	65.88	0.6227	0.6233
	DiffBIR-50 [31]	24.75	0.6567	0.2312	5.5346	64.98	0.6243	0.6463
	SeeSR-50 [29]	25.21	0.7216	0.2218	5.3970	69.70	0.6428	0.6673
	OSEDiff-1 [28]	25.15	0.7341	0.2128	5.6521	69.08	0.6326	0.6698
	PiSA-SR-1 [32]	25.50	0.7418	0.2044	5.5054	70.15	0.6552	0.6698
	SCR-1 (Ours)	25.34	0.7219	0.2149	5.2387	70.27	0.6689	0.6718
DIV2K	StableSR-200 [30]	23.26	0.5726	0.2048	4.7581	65.92	0.6188	0.6771
	DiffBIR-50 [31]	23.64	0.5647	0.2128	4.7042	65.81	0.6210	0.6704
	SeeSR-50 [29]	23.73	0.6056	0.1966	4.7903	68.42	0.6220	0.6867
	OSEDiff-1 [28]	23.72	0.6109	0.1975	4.7108	67.96	0.6147	0.6680
	PiSA-SR-1 [32]	23.86	0.6058	0.1934	4.5555	69.67	0.6401	0.6928
	SCR-1 (Ours)	23.75	0.6029	0.2231	4.5793	70.02	0.6561	0.6971



Figure 5: Comparison of restoration results of different Real-IR methods, the above samples are from RealSR (left) and DIV2K (right) datasets. Red boxes highlight zoom-in areas; yellow boxes indicate ground truth. Please zoom in for clarity.

Effectiveness of Semantic Restoration in Table 3. To assess semantic restoration, we compare the restoration results of OSEDiff, OSEDiff⁺ (inspired by PiSA-SR [32] with a frozen VAE encoder), and our SCR model on the degraded ADE20K dataset, and their performance on downstream segmentation tasks (R2S setting), with RASS as the segmentation model, as it achieves the best performance in R2S in Table 1. SCR introduces a semantically constrained loss aligned with segmentation priors and achieves the best performance, indicating improved visual and semantic consistency.

Table 3: Segmentation and restoration results on ADE20K-val under simulated degradation. Symbol ‘+’ denotes an enhanced version. Best results are highlighted in **bold**.

Method	mIoU \uparrow	LPIPS \downarrow	DISTS \downarrow	MUSIQ \uparrow	MANIQA \uparrow
OSEDiff	46.05	0.2731	0.1625	62.95	0.6506
OSEDiff ⁺	46.24	0.2653	0.1613	64.93	0.6702
SCR (Ours)	46.81	0.2628	0.1595	65.46	0.6746

Table 4: Ablation results of RAS on the restoration adaptations. All experiments are tested on degraded ADE20K dataset. Symbol ⁺ denotes an enhanced version. Best results are highlighted in **bold**.

Restoration Adaptation	mIoU \uparrow
None	44.56
OSEDiff ⁺	47.05
SCR (Ours)	47.42

Effectiveness of Restoration Adaptation in Table 4. To evaluate restoration adaptation, we test RASS with three variants: no restoration prior (None), OSEDiff⁺, and SCR, all using LQ images as input. It’s worth noting that in the “None” setting, we omit the first stage SCR model (restoration adaptation) and directly train the RAS model on the pre-trained T2I backbone. RASS consistently outperforms the others, confirming the benefit of integrating restoration into segmentation.

Table 5: Ablation results of SCR model on the additional description (AD). All experiments are tested on the DrealSR dataset.

Train	Testing	LPIPS \downarrow	DISTS \downarrow	MUSIQ \uparrow	MANIQA \uparrow
w/o AD	w/o AD	0.3143	0.2365	66.82	0.6338
w/ AD	w/o AD	0.3094	0.2302	67.15	0.6393
w/ AD	w/ AD	0.3094	0.2302	67.16	0.6394

Effectiveness of Additional Descriptive in Table 5. As stated in Section 3.2, we use RAM as an optional module to extract additional descriptive labels during training, while DAPE is employed at the inference stage. To evaluate the impact of descriptive inputs, we compare models trained using only category names with those trained using RAM-generated descriptions. While incorporating additional descriptions (w/ AD) leads to consistent performance improvements, the model remains stable even without such descriptions (w/o AD) during training. Moreover, enabling or disabling AD at inference results in only marginal performance variations. Based on these observations, we adopt additional descriptions by default.

Table 6: Ablation results of RAS model on the VAE features. All experiments are tested on the degraded ADE20K dataset.

UNet Features	VAE Encoder Features	VAE Decoder Features	mIoU	FPS	Params
✓	✗	✗	46.85	3.8	1788.1M
✓	✓	✗	47.42	3.4	1788.7M
✓	✗	✓	47.25	2.5	1788.6M
✓	✓	✓	47.60	2.4	1789.3M

Effectiveness of VAE Features. Table 6 demonstrates the impact of VAE features on segmentation. While decoder features are beneficial for segmentation, the decoder-side option introduces a significant runtime overhead: the inference speed drops from 3.4 FPS to 2.5 FPS (approximately a 30% reduction), which is mainly due to the computationally intensive upsampling operations involved in the VAE decoder. Considering the trade-off between performance and efficiency, we do not use decoder features by default.

5 Discussion

Despite the promising results, the large parameter size of our RASS model (due to its use of the pre-trained SD model) poses challenges for efficient inference. In addition, small object segmentation remains challenging, as the SD training strategy compresses features into the latent space via VAE, often discarding critical details essential for identifying small targets. Future work will focus on enhancing efficiency and improving small object detection capabilities. We plan to explore lightweight unified architectures to reduce inference costs. Additionally, we will investigate multi-scale feature reconstruction and high-resolution refinement strategies to better preserve fine details and improve segmentation performance for small objects.

6 Conclusion

We proposed RASS, a unified framework designed to improve the semantic segmentation performance of LQ images, which bridged image restoration and segmentation through LoRA-based module merging and task-specific fine-tuning. By incorporating semantic priors into the image restoration process, our unified framework achieved semantically meaningful and visually consistent reconstructions that benefit downstream segmentation. To support real-world applicability, we constructed a high-quality annotated dataset of real LQ images. Extensive experiments on both synthetic and real LQ benchmarks showed that our method achieved SOTA performance in both restoration and segmentation, validating the effectiveness of RASS.

7 Data Availability

The data that support the findings of this study are openly available at the following links corresponding to each dataset: <https://ade20k.csail.mit.edu/> (ADE20k), <https://osoundof.github.io/lmdir-data/> (LSDIR), <https://github.com/csjcai/RealSR> (RealSR), <https://github.com/xiezw5/Component-Divide-and-Conquer-for-Real-World-Image-Super-Resolution> (DrealSR), and <https://data.vision.ee.ethz.ch/cvl/DIV2K/> (DIV2K). All datasets are accessed in accordance with their respective official usage licenses, and no restricted access or additional permissions are required for academic research purposes as specified by each dataset's owner. The RealLQ dataset can be obtained through <https://github.com/Ka1Guan/RASS.git>.

References

- [1] Bowen Cheng, Alex Schwing, and Alexander Kirillov. Per-pixel classification is not all you need for semantic segmentation. *Advances in neural information processing systems*, 34:17864–17875, 2021.
- [2] Bowen Cheng, Ishan Misra, Alexander G Schwing, Alexander Kirillov, and Rohit Girdhar. Masked-attention mask transformer for universal image segmentation. In *Proceedings of the IEEE/CVF conference on computer vision and pattern recognition*, pages 1290–1299, 2022.
- [3] Yanming Guo, Yu Liu, Theodoros Georgiou, and Michael S Lew. A review of semantic segmentation using deep neural networks. *International journal of multimedia information retrieval*, 7:87–93, 2018.
- [4] Robin Strudel, Ricardo Garcia, Ivan Laptev, and Cordelia Schmid. Segmener: Transformer for semantic segmentation. In *Proceedings of the IEEE/CVF international conference on computer vision*, pages 7262–7272, 2021.
- [5] Yujian Mo, Yan Wu, Xinneng Yang, Feilin Liu, and Yujun Liao. Review the state-of-the-art technologies of semantic segmentation based on deep learning. *Neurocomputing*, 493:626–646, 2022.
- [6] Markus Hofmarcher, Thomas Unterthiner, José Arjona-Medina, Günter Klambauer, Sepp Hochreiter, and Bernhard Nessler. Visual scene understanding for autonomous driving using semantic segmentation. *Explainable AI: Interpreting, Explaining and Visualizing Deep Learning*, pages 285–296, 2019.
- [7] Liyi Chen, Chenyang Lei, Ruihuang Li, Shuai Li, Zhaoxiang Zhang, and Lei Zhang. Fpr: False positive rectification for weakly supervised semantic segmentation. In *Proceedings of the IEEE/CVF International Conference on Computer Vision*, pages 1108–1118, 2023.
- [8] Jonathan Long, Evan Shelhamer, and Trevor Darrell. Fully convolutional networks for semantic segmentation. In *Proceedings of the IEEE conference on computer vision and pattern recognition*, pages 3431–3440, 2015.
- [9] Liang-Chieh Chen, Yukun Zhu, George Papandreou, Florian Schroff, and Hartwig Adam. Encoder-decoder with atrous separable convolution for semantic image segmentation. In *Proceedings of the European conference on computer vision (ECCV)*, pages 801–818, 2018.
- [10] Olaf Ronneberger, Philipp Fischer, and Thomas Brox. U-net: Convolutional networks for biomedical image segmentation. In *Medical Image Computing and Computer-Assisted Intervention–MICCAI 2015: 18th International Conference, Munich, Germany, October 5–9, 2015, Proceedings, Part III 18*, pages 234–241. Springer, 2015.
- [11] Vijay Badrinarayanan, Alex Kendall, and Roberto Cipolla. Segnet: A deep convolutional encoder-decoder architecture for image segmentation. *IEEE transactions on pattern analysis and machine intelligence*, 39(12):2481–2495, 2017.
- [12] Enze Xie, Wenhui Wang, Zhiding Yu, Anima Anandkumar, Jose M Alvarez, and Ping Luo. Segformer: Simple and efficient design for semantic segmentation with transformers. In *Neural Information Processing Systems (NeurIPS)*, 2021.

[13] Zhenliang Ni, Xinghao Chen, Yingjie Zhai, Yehui Tang, and Yunhe Wang. Context-guided spatial feature reconstruction for efficient semantic segmentation. In *European Conference on Computer Vision*, pages 239–255. Springer, 2024.

[14] Liang-Chieh Chen, George Papandreou, Iasonas Kokkinos, Kevin Murphy, and Alan L Yuille. Deeplab: Semantic image segmentation with deep convolutional nets, atrous convolution, and fully connected crfs. *IEEE transactions on pattern analysis and machine intelligence*, 40(4):834–848, 2017.

[15] Jingyun Liang, Jiezhang Cao, Guolei Sun, Kai Zhang, Luc Van Gool, and Radu Timofte. Swinir: Image restoration using swin transformer. In *Proceedings of the IEEE/CVF international conference on computer vision*, pages 1833–1844, 2021.

[16] Jinghao Zhang, Jie Huang, Mingde Yao, Zizheng Yang, Hu Yu, Man Zhou, and Feng Zhao. Ingredient-oriented multi-degradation learning for image restoration. In *Proceedings of the IEEE/CVF conference on computer vision and pattern recognition*, pages 5825–5835, 2023.

[17] Wei-Ting Chen, Yu-Jiet Vong, Sy-Yen Kuo, Sizhou Ma, and Jian Wang. Robustsam: Segment anything robustly on degraded images. In *Proceedings of the IEEE/CVF Conference on Computer Vision and Pattern Recognition*, pages 4081–4091, 2024.

[18] Alexander Kirillov, Eric Mintun, Nikhila Ravi, Hanzi Mao, Chloe Rolland, Laura Gustafson, Tete Xiao, Spencer Whitehead, Alexander C Berg, Wan-Yen Lo, et al. Segment anything. In *Proceedings of the IEEE/CVF international conference on computer vision*, pages 4015–4026, 2023.

[19] Paul Couairon, Loick Chambon, Louis Serrano, Jean-Emmanuel Haugéard, Matthieu Cord, and Nicolas Thome. Jafar: Jack up any feature at any resolution. 2025.

[20] Stephanie Fu, Mark Hamilton, Laura Brandt, Axel Feldman, Zhoutong Zhang, and William T Freeman. Featup: A model-agnostic framework for features at any resolution. *The Twelfth International Conference on Learning Representations*, 2024.

[21] Xiangtao Kong, Xina Liu, Jinjin Gu, Yu Qiao, and Chao Dong. Reflash dropout in image super-resolution. In *Proceedings of the IEEE/CVF Conference on Computer Vision and Pattern Recognition*, pages 6002–6012, 2022.

[22] Xiangyu Chen, Xintao Wang, Wenlong Zhang, Xiangtao Kong, Yu Qiao, Jiantao Zhou, and Chao Dong. Hat: Hybrid attention transformer for image restoration. *IEEE Transactions on Pattern Analysis and Machine Intelligence*, 2025.

[23] Jeya Maria Jose Valanarasu, Rajeev Yasarla, and Vishal M Patel. Transweather: Transformer-based restoration of images degraded by adverse weather conditions. In *Proceedings of the IEEE/CVF conference on computer vision and pattern recognition*, pages 2353–2363, 2022.

[24] Yuanbiao Gou, Haiyu Zhao, Boyun Li, Xinyan Xiao, and Xi Peng. Test-time degradation adaptation for open-set image restoration. *arXiv preprint arXiv:2312.02197*, 2023.

[25] Ziwei Luo, Fredrik K Gustafsson, Zheng Zhao, Jens Sjölund, and Thomas B Schön. Controlling vision-language models for universal image restoration. *The Twelfth International Conference on Learning Representations*, 2024.

[26] Dazhou Guo, Yanting Pei, Kang Zheng, Hongkai Yu, Yuhang Lu, and Song Wang. Degraded image semantic segmentation with dense-gram networks. *IEEE Transactions on Image Processing*, 29:782–795, 2019.

[27] Robin Rombach, Andreas Blattmann, Dominik Lorenz, Patrick Esser, and Björn Ommer. High-resolution image synthesis with latent diffusion models, 2021.

[28] Rongyuan Wu, Lingchen Sun, Zhiyuan Ma, and Lei Zhang. One-step effective diffusion network for real-world image super-resolution. *Advances in Neural Information Processing Systems*, 37:92529–92553, 2024.

[29] Rongyuan Wu, Tao Yang, Lingchen Sun, Zhengqiang Zhang, Shuai Li, and Lei Zhang. Seesr: Towards semantics-aware real-world image super-resolution. In *Proceedings of the IEEE/CVF conference on computer vision and pattern recognition*, pages 25456–25467, 2024.

[30] Jianyi Wang, Zongsheng Yue, Shangchen Zhou, Kelvin CK Chan, and Chen Change Loy. Exploiting diffusion prior for real-world image super-resolution. *International Journal of Computer Vision*, 132(12):5929–5949, 2024.

[31] Xinqi Lin, Jingwen He, Ziyan Chen, Zhaoyang Lyu, Ben Fei, Bo Dai, Wanli Ouyang, Yu Qiao, and Chao Dong. Diffbir: Towards blind image restoration with generative diffusion prior. *Proceedings of the European conference on computer vision (ECCV)*, 2024.

[32] Lingchen Sun, Rongyuan Wu, Zhiyuan Ma, Shuaizheng Liu, Qiaosi Yi, and Lei Zhang. Pixel-level and semantic-level adjustable super-resolution: A dual-lora approach. In *Proceedings of the Computer Vision and Pattern Recognition Conference*, pages 2333–2343, 2025.

[33] Xuejing Niu, Bo Yan, Weimin Tan, and Junyi Wang. Effective image restoration for semantic segmentation. *Neurocomputing*, 374:100–108, 2020.

[34] Sohyun Lee, Namyup Kim, Sungyeon Kim, and Suha Kwak. Frest: Feature restoration for semantic segmentation under multiple adverse conditions. In *European Conference on Computer Vision*, pages 1–18. Springer, 2024.

[35] Jae-hun Shim, Hyunwoo Yu, Kyeongbo Kong, and Suk-Ju Kang. Feedformer: Revisiting transformer decoder for efficient semantic segmentation. In *Proceedings of the AAAI Conference on Artificial Intelligence*, volume 37, pages 2263–2271, 2023.

[36] Qiang Wan, Zilong Huang, Jiachen Lu, Gang Yu, and Li Zhang. Seaformer++: Squeeze-enhanced axial transformer for mobile visual recognition. *International Journal of Computer Vision*, pages 1–22, 2025.

[37] Jaeha Kim, Junghun Oh, and Kyoung Mu Lee. Beyond image super-resolution for image recognition with task-driven perceptual loss. In *Proceedings of the IEEE/CVF Conference on Computer Vision and Pattern Recognition*, pages 2651–2661, 2024.

[38] Kazuki Endo, Masayuki Tanaka, and Masatoshi Okutomi. Semantic segmentation of degraded images using layer-wise feature adjustor. In *Proceedings of the IEEE/CVF Winter Conference on Applications of Computer Vision*, pages 3205–3213, 2023.

[39] Yufei Wang, Wenhan Yang, Xinyuan Chen, Yaohui Wang, Lanqing Guo, Lap-Pui Chau, Ziwei Liu, Yu Qiao, Alex C Kot, and Bihan Wen. Sinsr: diffusion-based image super-resolution in a single step. In *Proceedings of the IEEE/CVF conference on computer vision and pattern recognition*, pages 25796–25805, 2024.

[40] Rongyuan Wu, Lingchen Sun, Zhiyuan Ma, and Lei Zhang. One-step effective diffusion network for real-world image super-resolution. *Advances in Neural Information Processing Systems*, 37:92529–92553, 2025.

[41] Edward J Hu, Yelong Shen, Phillip Wallis, Zeyuan Allen-Zhu, Yuanzhi Li, Shean Wang, Lu Wang, Weizhu Chen, et al. Lora: Low-rank adaptation of large language models. *ICLR*, 1(2):3, 2022.

[42] Youcai Zhang, Xinyu Huang, Jinyu Ma, Zhaoyang Li, Zhaochuan Luo, Yanchun Xie, Yuzhuo Qin, Tong Luo, Yaqian Li, Shilong Liu, et al. Recognize anything: A strong image tagging model. In *Proceedings of the IEEE/CVF Conference on Computer Vision and Pattern Recognition*, pages 1724–1732, 2024.

[43] Fausto Milletari, Nassir Navab, and Seyed-Ahmad Ahmadi. V-net: Fully convolutional neural networks for volumetric medical image segmentation. In *2016 fourth international conference on 3D vision (3DV)*, pages 565–571. Ieee, 2016.

[44] Bolei Zhou, Hang Zhao, Xavier Puig, Sanja Fidler, Adela Barriuso, and Antonio Torralba. Scene parsing through ade20k dataset. In *Proceedings of the IEEE conference on computer vision and pattern recognition*, pages 633–641, 2017.

[45] Xintao Wang, Liangbin Xie, Chao Dong, and Ying Shan. Real-esrgan: Training real-world blind super-resolution with pure synthetic data. In *Proceedings of the IEEE/CVF international conference on computer vision*, pages 1905–1914, 2021.

[46] Jianrui Cai, Hui Zeng, Hongwei Yong, Zisheng Cao, and Lei Zhang. Toward real-world single image super-resolution: A new benchmark and a new model. In *Proceedings of the IEEE/CVF international conference on computer vision*, pages 3086–3095, 2019.

[47] Pengxu Wei, Ziwei Xie, Hannan Lu, Zongyuan Zhan, Qixiang Ye, Wangmeng Zuo, and Liang Lin. Component divide-and-conquer for real-world image super-resolution. In *Computer Vision–ECCV 2020: 16th European Conference, Glasgow, UK, August 23–28, 2020, Proceedings, Part VIII 16*, pages 101–117. Springer, 2020.

[48] Xuaner Zhang, Qifeng Chen, Ren Ng, and Vladlen Koltun. Zoom to learn, learn to zoom. In *Proceedings of the IEEE/CVF Conference on Computer Vision and Pattern Recognition*, pages 3762–3770, 2019.

[49] Yawei Li, Kai Zhang, Jingyun Liang, Jiezheng Cao, Ce Liu, Rui Gong, Yulun Zhang, Hao Tang, Yun Liu, Denis Demedolx, et al. Lsdir: A large scale dataset for image restoration. In *Proceedings of the IEEE/CVF Conference on Computer Vision and Pattern Recognition*, pages 1775–1787, 2023.

[50] Eirikur Agustsson and Radu Timofte. Ntire 2017 challenge on single image super-resolution: Dataset and study. In *Proceedings of the IEEE conference on computer vision and pattern recognition workshops*, pages 126–135, 2017.

[51] Ilya Loshchilov and Frank Hutter. Decoupled weight decay regularization. *The Seventh International Conference on Learning Representations*, 2019.

[52] Zhou Wang, Alan C Bovik, Hamid R Sheikh, and Eero P Simoncelli. Image quality assessment: from error visibility to structural similarity. *IEEE transactions on image processing*, 13(4):600–612, 2004.

[53] Keyan Ding, Kede Ma, Shiqi Wang, and Eero P Simoncelli. Image quality assessment: Unifying structure and texture similarity. *IEEE transactions on pattern analysis and machine intelligence*, 44(5):2567–2581, 2020.

[54] Lin Zhang, Lei Zhang, and Alan C Bovik. A feature-enriched completely blind image quality evaluator. *IEEE Transactions on Image Processing*, 24(8):2579–2591, 2015.

[55] Sidi Yang, Tianhe Wu, Shuwei Shi, Shanshan Lao, Yuan Gong, Mingdeng Cao, Jiahao Wang, and Yujiu Yang. Maniqa: Multi-dimension attention network for no-reference image quality assessment. In *Proceedings of the IEEE/CVF Conference on Computer Vision and Pattern Recognition*, pages 1191–1200, 2022.

[56] Junjie Ke, Qifei Wang, Yilin Wang, Peyman Milanfar, and Feng Yang. Musiq: Multi-scale image quality transformer. In *Proceedings of the IEEE/CVF International Conference on Computer Vision*, pages 5148–5157, 2021.

[57] Qiang Wan, Zilong Huang, Jiachen Lu, YU Gang, and Li Zhang. Seaformer: Squeeze-enhanced axial transformer for mobile semantic segmentation. In *The eleventh international conference on learning representations*, 2023.

[58] Niccolo Cavagnero, Gabriele Rosi, Claudia Cuttano, Francesca Pistilli, Marco Ciccone, Giuseppe Averta, and Fabio Cermelli. Pem: Prototype-based efficient maskformer for image segmentation. In *Proceedings of the IEEE/CVF conference on computer vision and pattern recognition*, pages 15804–15813, 2024.

[59] Shuwei Ji and Hongyuan Zhang. ISAT with Segment Anything: An Interactive Semi-Automatic Annotation Tool, 2024. URL https://github.com/yatengLG/ISAT_with_segment_anything. Updated on 2025-02-07.

[60] Chaofeng Chen and Jiadi Mo. IQA-PyTorch: Pytorch toolbox for image quality assessment. [Online]. Available: <https://github.com/chaofengc/IQA-PyTorch>, 2022.

[61] Chaofeng Chen, Jiadi Mo, Jingwen Hou, Haoning Wu, Liang Liao, Wenxiu Sun, Qiong Yan, and Weisi Lin. Topiq: A top-down approach from semantics to distortions for image quality assessment. *IEEE Transactions on Image Processing*, 33:2404–2418, 2024.

[62] Nils Reimers and Iryna Gurevych. Sentence-bert: Sentence embeddings using siamese bert-networks. In *Proceedings of the 2019 Conference on Empirical Methods in Natural Language Processing*. Association for Computational Linguistics, 2019.

[63] Kai Zhang, Jingyun Liang, Luc Van Gool, and Radu Timofte. Designing a practical degradation model for deep blind image super-resolution. In *Proceedings of the IEEE/CVF international conference on computer vision*, pages 4791–4800, 2021.

[64] Jie Liang, Hui Zeng, and Lei Zhang. Details or artifacts: A locally discriminative learning approach to realistic image super-resolution. In *Proceedings of the IEEE/CVF conference on computer vision and pattern recognition*, pages 5657–5666, 2022.

[65] Chaofeng Chen, Xinyu Shi, Yipeng Qin, Xiaoming Li, Xiaoguang Han, Tao Yang, and Shihui Guo. Real-world blind super-resolution via feature matching with implicit high-resolution priors. In *Proceedings of the 30th ACM International Conference on Multimedia*, pages 1329–1338, 2022.

[66] Maxime Oquab, Timothée Darcet, Théo Moutakanni, Huy Vo, Marc Szafraniec, Vasil Khalidov, Pierre Fernandez, Daniel Haziza, Francisco Massa, Alaaeldin El-Nouby, et al. Dinov2: Learning robust visual features without supervision. *Transactions on Machine Learning Research*, 2024.

8 Appendices

In the file, we provide the following materials:

- *RealQ Dataset Setup*. More details of the collection of RealQ.
- *Mapping Table Setup*. More details of the mapping table.
- *Ablation Studies*. Ablation experiments of SCR training and hyperparameter selection on SCL.
- *Visualization Results*. Cross-attention map visualization analysis and visual comparisons.

8.1 RealQ Dataset Setup

To evaluate the generalization capability of the proposed RASS on real-world low-quality images, we introduce a new dataset named RealQ. Benefiting from the outstanding work of RealSR [46], DRealSR [47], and SR-Raw [48], we collect 100 LQ-HQ image pairs from these datasets. Pixel-level semantic annotations are conducted on the HQ images



Figure 6: RealLQ category statistics and some sample displays.

using an annotation assistance tool ‘ISAT’ [59] and manually fine-tuned, ensuring that the semantic labels are well aligned with the corresponding objects in the LQ images. The annotation categories follow the 150-class ADE20K taxonomy (100 “things” and 50 “stuff”), and across the 100 images. A total of 82 distinct categories are annotated, covering both indoor and outdoor scenes. All LQ images are resized to a short side of 512 pixels, with the segmentation maps correspondingly aligned. As a dedicated benchmark for real-world low-quality image segmentation, RealLQ helps bridge the gap in this underexplored area. Dataset samples and statistics are shown in Figure 6.

8.2 Ablation Study

SCR Training Data. Through our experiments, we observe that only a small number of samples are required to effectively train the restoration model. As shown in Table 7, we evaluate the baseline restoration model (an improved version of OSEDiff with the VAE encoder frozen) using different amounts of training data. ‘All’ denotes the full LSDIR training set containing 84,991 images. We then randomly sample three subsets of 10,000, 2,000, and 1,000 images. The results show that, given the same training time, model performance remains relatively stable even with significantly reduced training data.

Table 7: Ablation results of SCR model on training data. All experiments are tested on the DrealSR dataset. ‘Size’ indicates the amount of training data from LSDIR (e.g., ‘all’ for all 84991 images, ‘475’ for 475 images), except for 518, which are from ADE20K.

Size	PSNR↑	SSIM↑	DISTS↓	NIQE↓	MUSIQ↑	MANIQA↑	CLIPQA↑
All	28.54	0.7932	0.2113	6.5518	64.51	0.5987	0.6730
10000	28.47	0.7868	0.2157	6.6124	64.95	0.6032	0.6761
2000	28.52	0.7874	0.2112	6.2926	64.86	0.6013	0.6683
1000	28.45	0.7852	0.2185	6.3278	64.17	0.5975	0.6700
475	27.43	0.7303	0.2457	5.9606	69.12	0.6569	0.7018
475+518	28.14	0.7762	0.2259	6.4879	66.73	0.6274	0.6883

Since high-quality images are more beneficial for training restoration models, and our SCR training data needs to provide sufficiently good closed-set segmentation masks (to facilitate downstream semantic segmentation tasks), we select 475 high-quality samples based on image quality assessment (IQA) scores and segmentation quality. Specifically, we use the *maniq-pipal* and *topiq_nr-flive* functions in ‘PYIQA Toolbox’ [60] to identify the 1,000 images with the highest MANIQA [55] and TOPIQA [61] scores from the entire LSDIR dataset. We then segment each image using Mask2Former to obtain a semantic segmentation map. Based on the completeness and richness of the segmentation results, we manually select 475 training images (with an average score of 0.7697 for MANIQA and 0.7632 for TOPIQA). Training with this subset yields strong results in no-reference metrics (e.g., NIQE, MUSIQ, MANIQA, CLIPQA), but shows a notable drop in full-reference metrics (e.g., PSNR, SSIM, DISTS). This decline likely stems from limited generalization due to the reduced data size and the fact that full-reference metrics rely more heavily on pixel-level similarity to the ground truth. In SD-based generative restoration, however, the ground-truth image is not always the clearest or most detailed, yet restored outputs are still expected to align stylistically with it.

To balance no-reference and full-reference performance and benefit downstream segmentation tasks, we augment the training set by introducing 518 images from the ADE20K dataset (also filtered based on MANIQA and TOPIQA), enhanced using a restoration model (OSEDiff) to improve their IQA scores (averaging 0.7147 MANIQA and 0.7536 TOPIQA). These images include precise human-annotated segmentation masks, which benefit SCR training. Ultimately, our training set consists of 475 LSDIR images and 518 enhanced ADE20K images. As shown in the results for the sample size of 475+518 in Table 7, this setting preserves strong no-reference metric performance while improving full-reference scores.

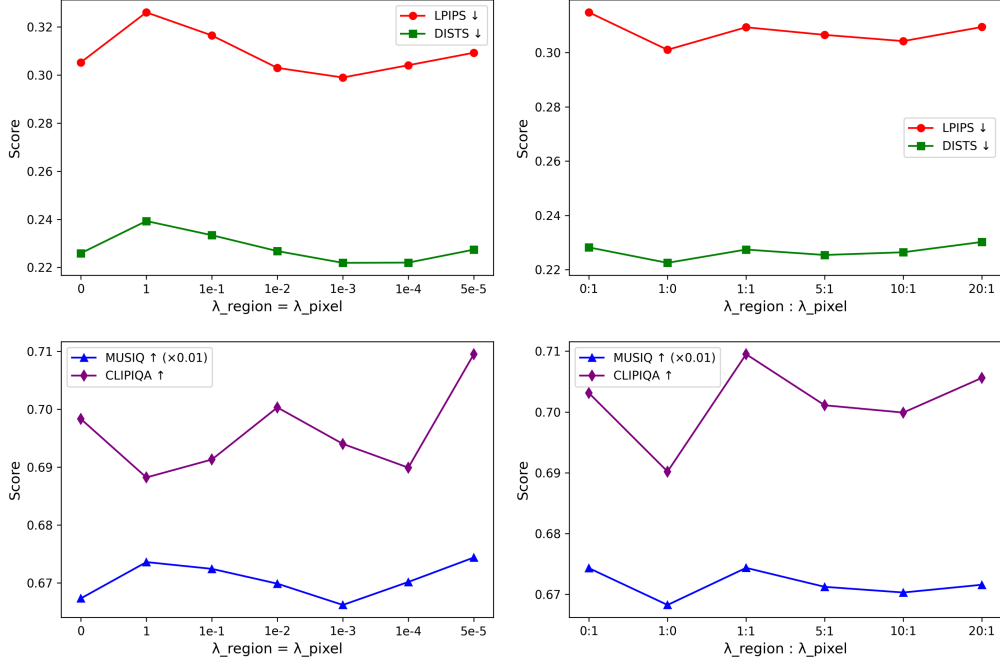


Figure 7: Comparison of different λ_{region} and λ_{pixel} settings. The quantization results from the DrealSR dataset.

Hyperparameters in Semantic-Constrained Loss. We perform ablation experiments on the two scaling factors, λ_{region} and λ_{pixel} , in Equation (2). We begin by setting both factors to the same value to assess the overall impact of scaling on model performance. As shown in the two line graphs on the left of Figure 7 (where 0 denotes the baseline model without the additional loss), the results suggest that smaller scaling factors are more favorable for training the restoration model. Building on this observation, we further investigate the balance between region-level and pixel-level losses. As illustrated in the two line charts on the right of Figure 7, using only region-level loss (*i.e.*, 1:0) or only pixel-level loss (*i.e.*, 0:1) yields inferior performance compared to a balanced combination of both. Based on these findings, we adopt $\lambda_{\text{region}} = 1e-3$ and $\lambda_{\text{pixel}} = 5e-5$ as the default configuration in all subsequent experiments.

8.3 Mapping Table Setup

To align the text descriptions extracted by RAM with the 150 semantic categories defined by Mask2Former and enable RAM-generated descriptions to inherit Mask2Former’s segmentation annotations, we construct a mapping table. Specifically, we first apply RAM to extract labels across the entire training dataset. We then employ a sentence similarity model Sentence-BERT [62] to compute the most semantically similar Mask2Former label for each RAM label and record the corresponding similarity score. Alignments with low confidence (similarity ≤ 0.5) are discarded and additional unreasonable matches are manually filtered out. A partial mapping table is presented in Table 8, and the complete version will be made publicly available in future releases.

8.4 Cross-Attention Map Visualization Analysis.

We visualize the cross-attention maps during the restoration process in Figure 8. The first column shows the aggregated cross-attention maps, obtained by merging all attention layers in the latent diffusion network. The second column presents the restored images, and the third column shows the RASS segmentation results of the restored image. It can be clearly observed that the restoration model with semantic constraints exhibits more accurate attention to semantically

Table 8: Partial mapping table display.

RAM-generated Word	Most Similar Word	Similarity Score↑
lake	lake	1.0000
blanket	blanket	0.8754
woman	person	0.6375
sit	seat	0.7008
stair	stairs	0.9246
home	house	0.8043
entrance	door	0.6537
doorway	door	0.7985
harbor	pier	0.6539
pond	lake	0.7054
...

meaningful regions, such as the ‘stairs’ area (third row). In contrast, the model without semantic constraints shows inaccurate attention, *e.g.*, responding to ‘building’ as ‘stairs’ area (second row), leading to coarse segmentation results. These observations highlight the effectiveness of SCL in enhancing the semantic fidelity of restoration and supporting downstream segmentation performance.

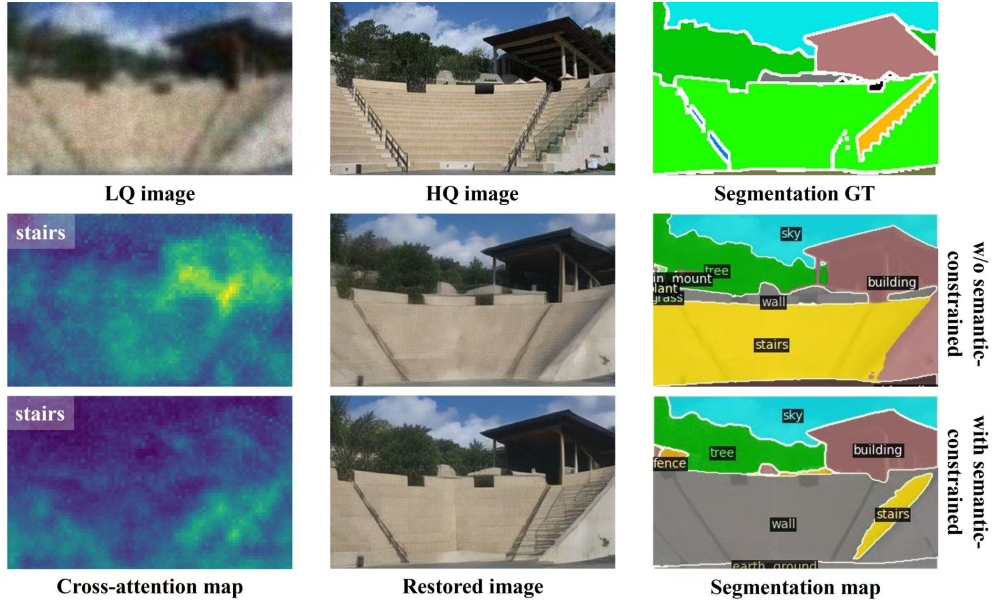


Figure 8: Cross-attention map visualization results. Sample is from ADE20K.

8.5 Comparison Results

We present quantitative comparison results between SCR and GAN-based models. In Table 9, we compare SCR with four representative GAN-based Real-ISR methods: BSRGAN [63], Real-ESRGAN [45], LDL [64], and FeMaSR [65]. Unsurprisingly, these GAN-based methods outperform SCR in terms of fidelity metrics such as PSNR and SSIM, while SCR achieves a clear advantage in perceptually limited metrics.

We present quantitative comparison results between RASS and feature-refinement method in Table 10, exemplified by JAFAR [19], which improves DINOv2-ViT-S/14 [66] (with bilinear upsampling) on SQ ADE20K from 39.23 to 40.49 mIoU. We consider three evaluation settings according to the quality of input images: Standard Quality (SQ), Simulated Degradation (SiD), and Real-World Degradation (RD). SQ images are from ADE20K; SiD images are obtained by applying the degradation pipeline of RealESRGAN to ADE20K; RD images are from our collected RealLQ dataset. We can see that RASS consistently outperforms the representative refinement based method JAFAR across SQ, SiD and RD settings, demonstrating that RASS is not limited to “rescue” cases but also yields large gains on standard quality

Table 9: Quantitative comparison with GAN-based methods on DrealSR, RealSR and DIV2K datasets. Best results are highlighted in **bold**.

Dataset	Method	PSNR↑	SSIM↑	DISTS↓	NIQE↓	MUSIQ↑	MANIQA↑	CLIPIQ↑
DrealSR	BSRGAN [63]	26.39	0.7654	0.2121	5.6567	63.21	0.5399	0.5001
	Real-ESRGAN [45]	25.69	0.7616	0.2063	5.8295	60.18	0.5487	0.4449
	LDL [64]	25.28	0.7567	0.2121	6.0024	60.82	0.5485	0.4477
	FeMASR [65]	25.07	0.7358	0.2288	5.7885	58.95	0.4865	0.5270
	SCR (Ours)	25.34	0.7219	0.2149	5.2387	70.27	0.6689	0.6718
RealSR	BSRGAN [63]	26.39	0.7654	0.2121	5.6567	63.21	0.5399	0.5001
	Real-ESRGAN [45]	25.69	0.7616	0.2063	5.8295	60.18	0.5487	0.4449
	LDL [64]	25.28	0.7567	0.2121	6.0024	60.82	0.5485	0.4477
	FeMASR [65]	25.07	0.7358	0.2288	5.7885	58.95	0.4865	0.5270
	SCR (Ours)	25.34	0.7219	0.2149	5.2387	70.27	0.6689	0.6718
DIV2K	BSRGAN [63]	24.58	0.6269	0.2275	4.7518	61.20	0.5071	0.5247
	Real-ESRGAN [45]	24.29	0.6371	0.2141	4.6786	61.06	0.5501	0.5277
	LDL [64]	23.83	0.6344	0.2227	4.8554	60.04	0.5350	0.5180
	FeMASR [65]	23.06	0.5887	0.2057	4.7410	60.83	0.5074	0.5997
	SCR (Ours)	23.73	0.6029	0.2231	4.5793	70.02	0.6561	0.6971

and mild–moderate degradations. However, we agree that the cost of RASS is higher than JAFAR (FPS 1.84 vs 8.13). Overall, the experiments support RASS as a general-purpose recovery module with certain cost in latency.

Table 10: Quantitative comparison with representative feature-refinement baseline (JAFAR). All FPS measured on NVIDIA A6000.

Method	ADE20K (SQ)		ADE20K (SiD)			RealLQ (RD)			FPS
	DT	DT	R2S	FT	DT	R2S	FT		
JAFAR [19]	40.49		23.91	34.82	28.01	17.77	18.40	20.23	8.13
RASS (Ours)	53.76	-	46.81	47.42	-	37.84	39.80	1.84	